

CFD METHODOLOGIES FOR A PWR FUEL ROD ASSEMBLY

Ted N. Blowe, Shin K. Kang, and Yassin A. Hassan
Department of Nuclear Engineering, Texas A&M University,
College Station, TX, 77843-3133, USA
tblowe@tamu.edu, paengki1@tamu.edu, y-hassan@tamu.edu

ABSTRACT

Although numerous applications of computational fluid dynamics (CFD) codes to predict turbulent flows and heat transfer in a pressurized water reactor (PWR) fuel rod assembly have been performed, most of them have not been fully validated mainly due to lack of high fidelity experimental data. However, NESTOR experiment performed by CEA-EDF-EPRI provided accurate data for various variables (mean and RMS axial velocities, and pressure drops) over a broad range in a 5×5 PWR fuel rod assembly with and without mixing vane grids (MVGs). This study considered the steady Reynolds Averaged Navier-Stokes (RANS) turbulence models because of its feasibility in application to the real PWR fuel rod bundle. Mesh size sensitivity studies investigated global base and axial mesh perturbations, with respect to a selected mesh refinement. Isotropic and anisotropic turbulence models with high y^+ wall function were examined. Furthermore, we investigated the importance of the anisotropic turbulence model in the typical PWR rod bundle by removing a SSG in-between two MVG spans. Axial and global mesh size sensitivity studies identified reasonable mesh refinements for various regions of the SSG and MVG span types. Examined turbulence models over predicted and slightly under predicted MVG and SSG pressure loss ratios, respectively. CFD-calculations produced comparable mean axial velocity (MVG and SSG spans) and RMS axial velocity fluctuation (MVG span) profiles with respect to experimental measurements. The SSG's main purpose in the MANIVEL-MVG bundle is to stabilize the 5×5 rod array between consecutive MVGs. Unintended or undesirable consequences of the SSG (in this problem) include; the observed presence of secondary flow structures in the SSG far wake region, the sudden reduction of cross-flow upon passing the SSG, and the re-distribution of wall shear stresses upon passing the SSG. Thus, the mere inclusion of SSGs in the MANIVEL MVG bundle introduces a basic limitation for validating CFD methodologies to a general PWR MVG bundle. Without the SSG between consecutive MVGs, cross-flow engendered by mixing-vanes was more dominant than the turbulence anisotropy-driven secondary flow along the MVG's wake region. This reduces the anisotropic turbulence model's relative importance in application to the actual PWR MVG bundle.

KEYWORDS

PWR 5×5 bundle assembly, Mixing Vane Grid, steady RANS, CFD validation

1. INTRODUCTION

In recent years, advances in PWR fuel performance have led to higher fuel burnup, longer fuel cycles, and power uprates. Demonstrating fuel reliability under these enhanced conditions is a key challenge for high-duty PWR cores. Failure to do so may increase shutdown frequency and limit operational freedom. Fuel failures and unexpected power shifts during operations are fuel reliability risk factors. A possible fuel failure mechanism and undesirable power shift mechanism are the occurrence of (i) crud-induced localized corrosion (CILC), and (ii) crud-induced power shift (CIPS previously called Axial Offset Anomaly), respectively. Sub-cooled nucleate boiling (SNB) in the upper region of a PWR core is known

to facilitate the build-up of corrosion products on fuel rod surfaces. Understanding local fuel rod bundle conditions is a necessary step for mitigating risk associated with CILC induced fuel failures and CIPS incidents.

Common PWR fuel assemblies span approximately four meters in height, and consist of a 17×17 square array of in-line fuel rods with constant pitch spacing between rods. Fuel rods are held in place by support grids placed along the fuel assembly. Support grids with mixing vanes at the end of grid straps, commonly referred to as MVGs; enhance turbulent mixing in the MVG wake region. Enhanced turbulent mixing helps prevent the occurrence of SNB by increasing the critical heat flux (CHF). Studying fluid dynamics and single-phase heat transfer characteristics for turbulent flows around PWR fuel rod bundles with complex split-type MVGs is crucial to predict local hot spots, i.e. potential SNB regions. Neither one dimensional system codes, nor sub-channel codes appropriately predict local hot spots. In contrast, CFD codes can analyze and resolve turbulent flow structures and local heat transfer characteristics within a fuel rod bundle. These CFD codes must be validated prior to practical thermal hydraulic application.

The objectives of this study include; (i) validating CFD methodologies (mesh size, boundary conditions, turbulence models) with experimental measurements; (ii) investigate how SSGs disrupt cross-flow effects introduced from MVGs; and (iii) investigate a longer MVG span (similar to a general PWR MVG bundle's wake region) by removing a SSG between two MVG spans. This study adopted the commercial software Star-CCM+ v9.04.009 [1], which uses a finite volume approach to solve the steady RANS equations.

2. Problem (NESTOR Experiment)

In the outlined framework, the CEA-EDF-EPRI collaborative NESTOR project [2] aimed to produce accurate thermal-hydraulic experimental data for 5×5 rod bundles with support grids. Characterization of grid pressure loss and axial velocity fields by Laser-Doppler Velocimetry (LDV) in single-phase flow was examined during hydraulic isothermal tests on the EDF-CHATOU MANIVEL loop considering bundle configurations with alternating MVGs of the Westinghouse V5H design and SSGs, as shown in Figure 1 and Figure 2. This study obtained MVG01 orientation from the counter-clockwise rotation of MVG02 orientation by 90° about the z-axis, as shown in Figure 3 (a) and (b), respectively. Isothermal test conditions were considered, as shown in Table I.

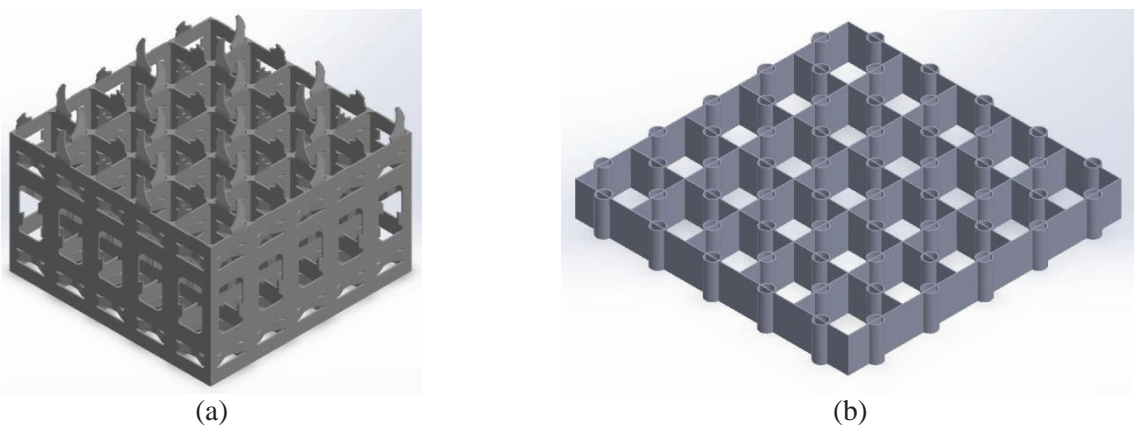


Figure 1 3D view of support grids: (a) Westinghouse V5H MVG and (b) simple support grid (SSG).

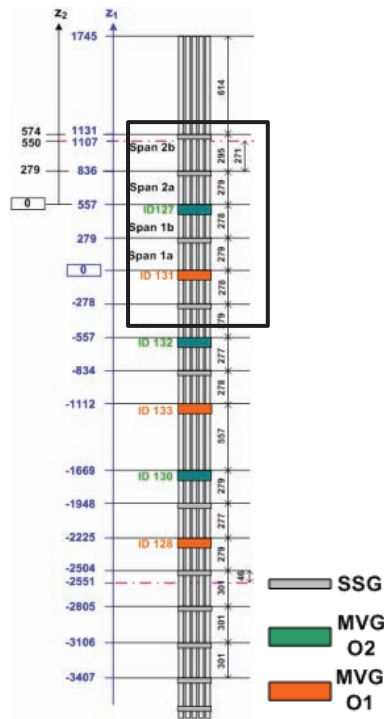


Figure 2 Axial configuration of MANIVEL MVG bundle (length in mm); [3].

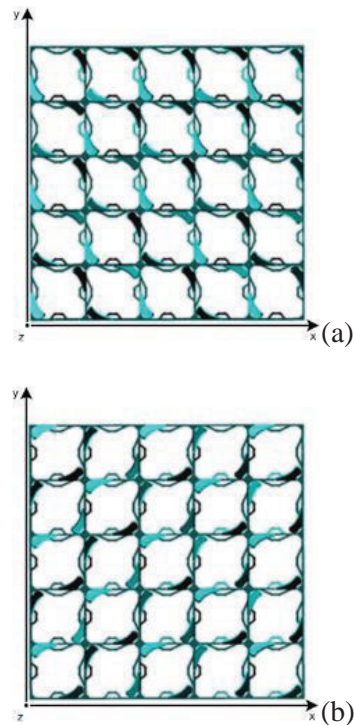


Figure 3 Westinghouse V5H MVG orientation; (a) MVG01, and (b) MVG02, [3].

Table I. Isothermal thermal hydraulic conditions

Outlet Pressure (bar)	Flow Rate (m ³ /h)	Outlet Temperature (°C)
1 bar	64.7	29.7

Mean axial velocity and RMS axial velocity fluctuation line profiles were compared along selected axial and lateral ranges, as shown in Table II and Figure 4.

Table II. MANIVEL-MVG bundle Mean axial velocity and RMS axial velocity fluctuation comparison locations; (a) axial range, and (b) lateral range.

(a)

Span	Axial Range (mm)
1a (z ₁)	25, 50, 75, 100, 175, 250
1b (z ₁)	304, 379, 514
2a (z ₂)	25, 50, 75, 100, 175, 210
2b (z ₂)	304, 379, 514

(b)

Lateral Range		
Line	x (mm)	y (mm)
1	26.6	0~66.1
2	39.1	0~66.1
3	0~66.1	26.6
4	0~66.1	39.1

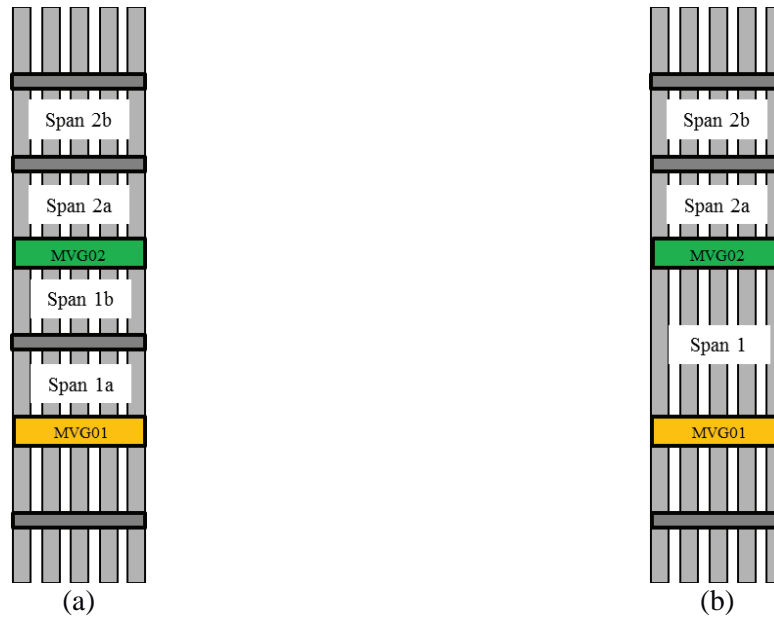


Figure 5 Adopted computational axial domains; (a) mesh sensitivity study, (b) numerical study.

3.2. Turbulence model with associated near-wall treatment

Isotropic and anisotropic turbulence models were adopted. The two-equation standard k - ϵ linear eddy viscosity model (std) with transport equations for turbulent kinetic energy and dissipation rate suggested by [5] and coefficients from [6] served as an isotropic turbulence model. Applying coefficients suggested by [7] to the quadratic k - ϵ turbulence model served as an anisotropic modified quadratic k - ϵ turbulence model (modQuad). Stated isotropic and anisotropic turbulence models adopted a wall function (high- y^+ treatment in the STAR-ccm+ code) for near-wall treatment.

3.3. Mesh

The computational domain was discretized with the Star-CCM+ mesh generation algorithm to construct an unstructured trimmed mesh. A hexahedral template grid is first applied to the domain, then the meshing algorithm trims or cuts the hexahedral template to accommodate geometric surfaces with prism layers extruded from the solid boundary for a more accurate near-wall value (called prism layers in this study)[1]. The adopted mesh generation process, mesh type, and mesh configuration have been used by others [4] for similar CFD methodology and validation applications regarding 5×5 rod bundle with support grid [3].

3.3.1. Mesh configuration

Due to the size and complexity of the MANIVEL MVG bundle problem, computation domain simplifications were adopted to reduce computational resources for large CFD calculations, while adequately resolving the following detailed geometric features; MVGs, SSGs, and near-wall regions. The core region of a support grid and adjacent bare-rod regions consist of uniform hexa and trimmed hexa cells with sufficient refinement near all walls. MVG and SSG span types, were sub-divided into three characteristic regions: (i) far wake upstream and downstream extruded bare-rod regions, (ii) near upstream and downstream refined regions, and (iii) grid region, as shown in Figure 6. Regions (i) and (ii) have the same lateral grid size, but grid points in region (i) are extruded in the axial direction in order to

reduce the total number of grid points. Region (iii) for SSG spans incorporates high refinement near all wall and core regions approximately one pin diameter upstream of the SSG bottom, within the SSG, and approximately two pin diameters upstream of the SSG top, as well as elongated grid point upstream and downstream of stated regions, as shown in Figure 3(a). Region (iii) for MVG spans incorporates high refinement near all walls and core regions approximately 1 pin diameter upstream of the MVG bottom, within the MVG, and approximately 6 pin diameters upstream of the MVG top, with elongated grid point upstream and downstream of stated regions, as shown in Figure 6. Individual MVG and SSG spans were combined to form the complete computational domain.

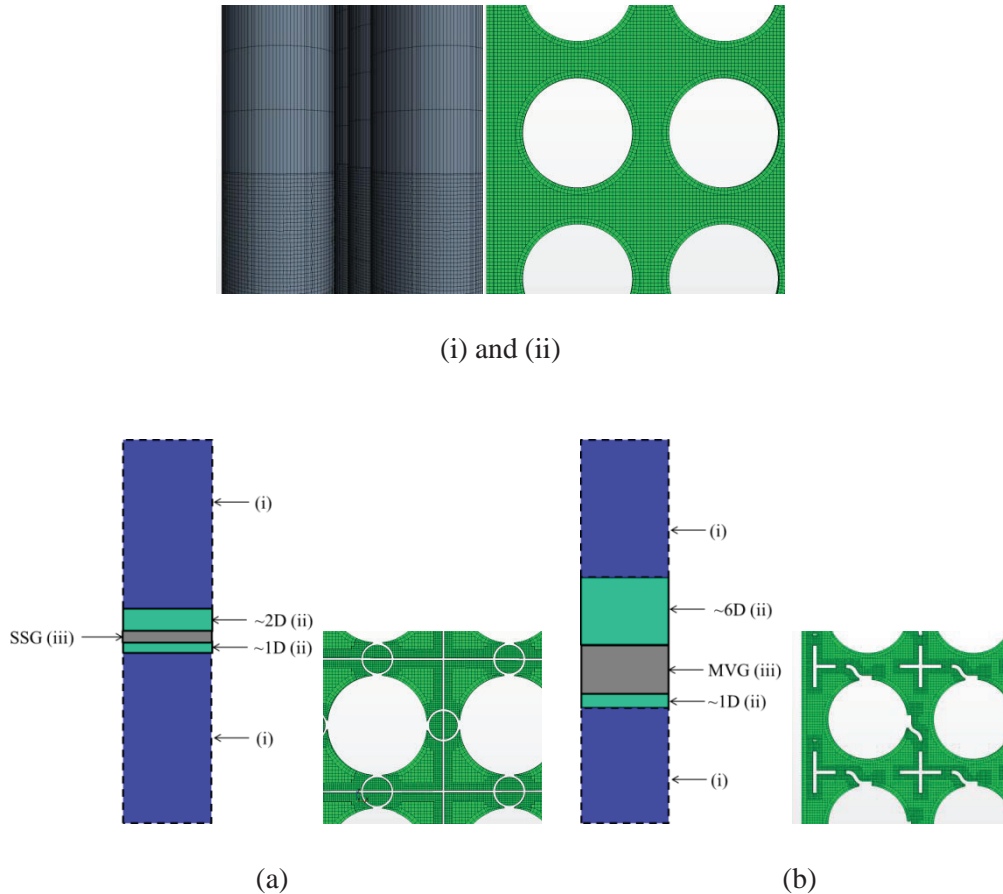


Figure 6 Mesh configuration for (a) SSG span and (b) MVG span.

3.3.2. Mesh sensitivity study

Adopting a sufficiently fine mesh for stated mesh configurations is required prior to making CFD-code-to-experiment comparisons. Mesh refinements were modified with respect to selected characteristic support grid span region [Figure 6] while keeping other CFD methodological considerations the same. Each mesh size sensitivity case adopted the computational domain show in Figure 5(a), isothermal operating conditions [Table I], and standard k- ϵ turbulence model with high- y^+ wall function.

Mesh size sensitivity studies examined extruded axial mesh size for region (i) [Figure 6], and global base mesh size for all regions [Figure 6 (a) and (b)], as shown in Table III and Table IV. Table III (a) describes the axial mesh refinement of extruded bare-rod cells within region (i), referred to as A# and axial size. Table III (b) describes the global base refinement for all regions (except extruded bare-rod cells within region (i)), referred to as B# and base size. The number of extruded prism layers from each rod and casing wall boundaries is listed in Table IV. Prism layers were not extruded from support grid walls. The near-wall regions adjacent to support grid walls are approximately half the listed base size. The volume ratio between axially adjacent cells at the axial mesh height discontinuity [Figure 6 (i)] is described for each mesh refinement, as shown in Table IV.

Table III. Mesh sensitivity size labels; (a) axial mesh length of extruded bare-rod cells within region (i) [axial], and (b) global base size for all regions [global].

(a)		(b)	
	Axial Size		Base Size
Label	(mm)	Label	(mm)
A3	9.50	B3	0.60
A2	4.75	B2	0.30
A1	2.38	B1	0.23

Table IV. Mesh sensitivity test matrix (a) axial, and (b) global.

(a)				(b)			
Mesh Label	Prism Layers	Volume Ratio	Total Cells (million)	Mesh Label	Prism Layers	Volume Ratio	Total Cells (million)
A3-B2	3	30.45	82.65	A2-B3	3	7.96	20.34
A2-B2	2	15.95	86.84	A2-B2	2	15.95	86.84
A1-B2	2	7.97	95.68	A2-B1	2	20.80	159.30

Mean axial velocity at point locations along stated axial and lateral ranges [Table II] were compared between stated mesh refinements to identify a sufficiently fine mesh for CFD-code-to-experiment benchmark comparisons. In order to compare mean axial velocity point values between significantly different mesh refinements, the extracted point value from each mesh refinement must have the same centroid within the spatial domain. If the centroids between mesh refinements are slightly different, then the extracted values will not correspond and institute an additional source of error. Accordingly, the solution from a finer mesh was mapped (least squares interpolation) onto the coarse mesh, so all extracted point centroids' correspond with the coarse mesh centroid. This method guaranteed that various mesh refinements' mean axial velocity point values shared the same centroid location.

4. RESULTS AND DISCUSSION

Dimensionless wall distance (y^+) was examined for rod and casing walls in all CFD calculations. Axial and global mesh size sensitivity studies compared mean axial velocity line profiles and approximate relative error between mesh refinements. As a result, CFD-calculations adopted a sufficiently fine mesh for CFD-code-to-experiment and turbulence model comparisons.

CFD-code-to-experiment comparisons considered the following validation benchmarks; grid-span pressure loss ratios, mean axial velocity profiles, RMS axial velocity profiles. To ensure a consistent pressure loss comparison between CFD and experimental results under different thermal hydraulic conditions, a one-span pressure loss coefficient (P_{loss}) defined as $P_{loss} = \Delta P_{1span} / (\frac{1}{2}\rho V_0^2)$ where ΔP_{1span} is measured or calculated one-span pressure loss; ρ is density, and V_0 is bulk velocity. Mean and RMS axial velocity profiles were compared along Line 3 in the wake of the grid region. RMS axial velocity fluctuation was calculated using the turbulence kinetic energy (K) $\sqrt{2K/3}$.

Computational domain (with and without the SSG between two MVG spans) and turbulence model considerations examined how cross-flow and wall shear stresses evolve along the MVG wake region. Cross-flow in terms of secondary flow intensity was examined as the flow progresses in Span 1 by averaging the secondary flow intensity for sub-channels surrounding Rod 5 (SC15, SC16, SC21, and SC22 [Figure 4]), as shown in Figure 14. Secondary flow intensity (FI_{2nd}) is defined as, $FI_{2nd} = \frac{1}{A} \int \frac{\sqrt{\bar{u}_x^2 + \bar{u}_y^2}}{\bar{u}_{z,bulk}} dA$, where A is the sub-channel area. Wall shear stresses around Rod 5 were normalized with respect to the elevation averaged value.

4.1. Dimensionless wall distance

Examined CFD-calculations adopted the high- y^+ wall treatment (law-of-the-wall), which assumes near-wall cells adjacent to no-slip boundaries are within the turbulent boundary layer's [1] logarithmic region. The physical basis of the law-of-the-wall loses accuracy across the support grid region as a result of the strong pressure gradient caused by the sudden reduction in flow area from bare-rod to support grid [8]. Consequently, the high- y^+ wall treatment has a basic limitation for this problem. Examined CFD calculations have y^+ values ranging from 30 to 100 for approximately 95% to 97% of near-wall cells adjacent to the rod and casing walls. Rod and casing walls have an average y^+ value between 50 and 55, respectively.

4.2. Mesh sensitivity studies

Mean axial velocity (v) approximate relative errors [equations 1, 2, and 3], and mean axial velocity profiles were examined between axial and global mesh size perturbations, with respect to mesh refinement A2-B2.

$$e_a^{A3A1} = \frac{1}{N} \sum_{i=1}^N \left| \frac{v_{A1B2i} - v_{A3B2i}}{v_{A1B2i}} \right|; e_a^{B3B1} = \frac{1}{N} \sum_{i=1}^N \left| \frac{v_{A2B1i} - v_{A2B3i}}{v_{A2B1i}} \right| \quad (1)$$

$$e_a^{A3A2} = \frac{1}{N} \sum_{i=1}^N \left| \frac{v_{A2B2i} - v_{A3B2i}}{v_{A2B2i}} \right|; e_a^{B3B2} = \frac{1}{N} \sum_{i=1}^N \left| \frac{v_{A2B2i} - v_{A2B3i}}{v_{A2B2i}} \right| \quad (2)$$

$$e_a^{A2A1} = \frac{1}{N} \sum_{i=1}^N \left| \frac{v_{A2B1i} - v_{A2B2i}}{v_{A2B1i}} \right|; e_a^{B2B1} = \frac{1}{N} \sum_{i=1}^N \left| \frac{v_{A2B1i} - v_{A2B2i}}{v_{A2B1i}} \right| \quad (3)$$

Axial mesh size perturbations indicated the following approximate relative percent errors; from A3-B2 to A1-B2 of 0.403%; from A3-B2 to A2-B2 of 0.346%; from A2-B2 to A1-B2 of 0.089%, as shown in Table V(a). Global base mesh size perturbations indicate the following approximate relative percent errors; from A2-B3 to A2-B1 of 1.632%; from A2-B3 to A2-B2 of 1.283%; from A2-B2 to A2-B1 of 0.741%, as shown in Table V (b).

Table V. Mean axial point velocity averaged approximate relative difference for Spans 1 and 2; (a) axial, and (b) global.

(a)		(b)	
$e_a^{A3A1}(\%)$	0.403	$e_a^{B3B1}(\%)$	1.632
$e_a^{A3A2}(\%)$	0.346	$e_a^{B3B2}(\%)$	1.283
$e_a^{A2A1}(\%)$	0.089	$e_a^{B2B1}(\%)$	0.741

Mean axial velocity profiles for axial mesh size refinements conveyed sensitivity to refinements in the axial length of extruded bare-rod cells for both MVG and SSG near (25mm) and intermediate (75mm) wake regions, as shown in Figure 7 (a) and (b), respectively. These sensitivity regions coincide with the first measured axial locations downstream of the mesh discontinuity, as shown in Figure 6. Comparisons for all other wake regions show negligible sensitivity between examined axial mesh refinements. Similarly, global base size refinements observed sensitivity in both MVG and SSG near wake regions (25mm), as shown in Figure 7 (c) and (d), respectively. Comparisons at all other wake regions show comparable sensitivity between examined global mesh refinements.

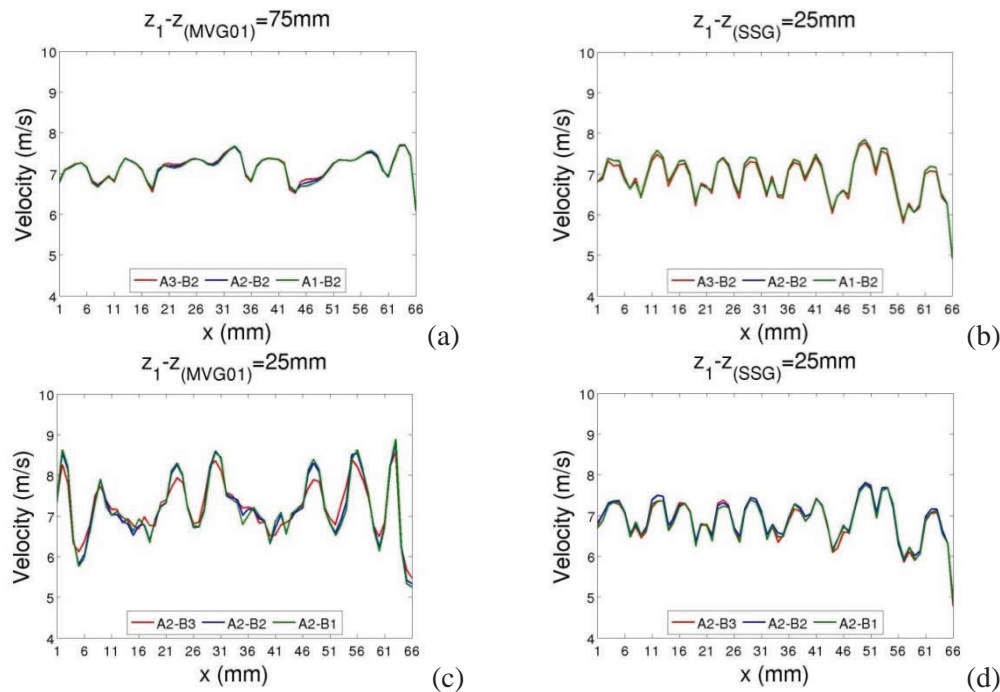


Figure 7 mean axial velocities comparisons along line 3 at selected axial heights in span 1; (a) axial MVG, (b) axial SSG, (c) global MVG, and (d) global SSG.

Approximate relative errors and mean axial velocity profiles between examined axial mesh refinements indicate only minor sensitivity to mean axial velocity values, even though the interfacial volume ration increases from ~8 to ~30 [Table III]. Similarly, A2-B3 to A2-B2 global base sizes indicate considerable sensitivity to mean axial velocity values, whereas stated values show less sensitivity between A2-B2 to A2-B1 refinements. CFD-to-experiment validation comparisons adopted 4.75mm and 0.30 mm for the axial length of extruded bare-rod cells and global base mesh size, respectively.

4.3. Grid Span Pressure Loss

The pressure loss ratio for each span type - MVG, SSG, bare-rod -from CFD-calculations were normalized with respect to the corresponding experimental pressure loss, as shown in Figure 8. For the MVG span, both modified quadratic k-ε and standard k-ε turbulence models over-predict the pressure loss ratio by ~10.2% and 13.1%, respectively. For the SSG span, both modified quadratic k-ε and standard k-ε turbulence models under-predict the pressure loss ratio by ~6.1% and ~3.0%, respectively. For the bare-rod span, both modified quadratic k-ε and standard k-ε turbulence models show good agreement with the measurement (under-prediction by ~0.5% and over-prediction of ~0.3%, respectively). The modified quadratic k-ε model shows slightly lower pressure losses for both MVG and SSG spans than standard k-ε model. This difference is due to the lower pressure loss across the grid, as opposed to the pressure gradient difference in the far wake region, as shown in Figure 8 (a) and (b).

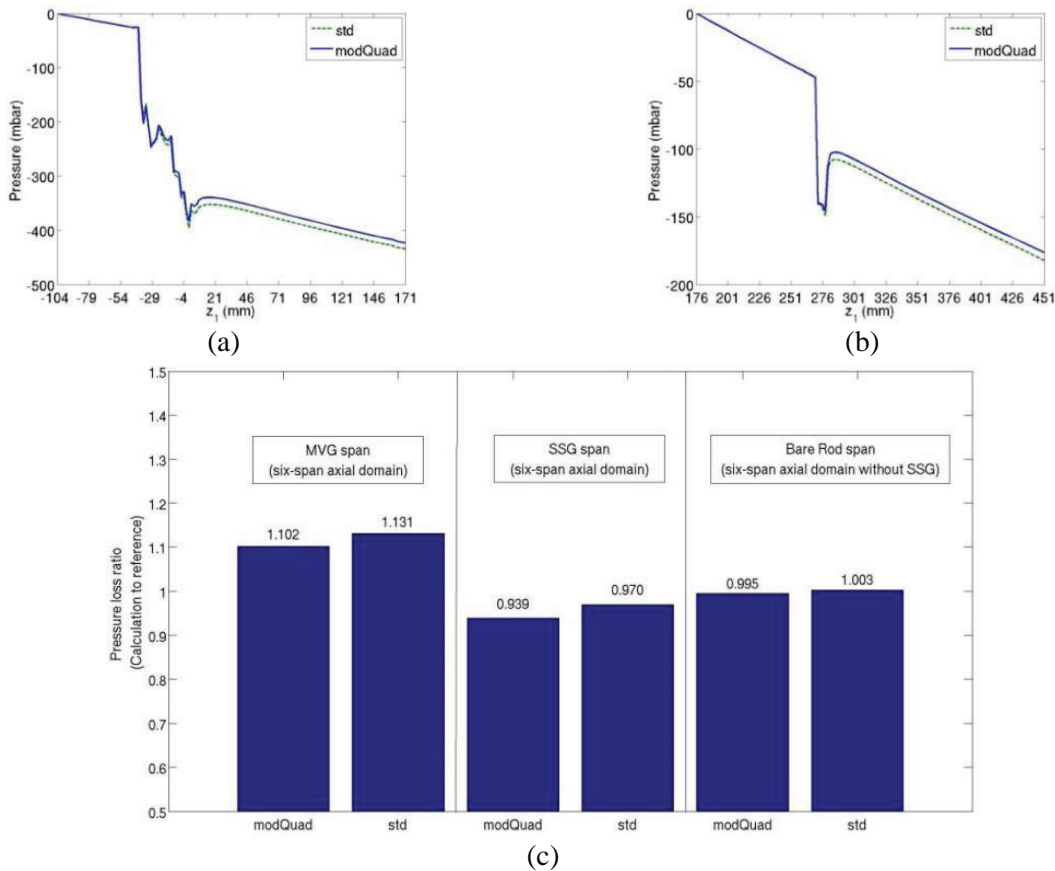


Figure 8 (a) MVG span axial pressure distribution (b) SSG span axial pressure distribution (c) Comparison of MVG, SSG, and bare-rod span pressure losses.

4.4. Flow Field, Secondary Flow Intensity, and Wall Shear Stress

4.4.1. Mean axial velocity in the MVG span

Isotropic, anisotropic, and experimental mean axial velocities were compared along line 3 at various elevations within the core region of span 1a, as shown in Figure 9. The overall distributions are comparable, but localized flow structure shows distinguishable discrepancies between CFD calculations and experimental results in the near and far downstream regions. The intermediate downstream region shows more comparable localized flow structure between CFD calculations and experimental results. Both standard $k-\epsilon$ and modified quadratic $k-\epsilon$ turbulence models show very similar results at all elevations for the MVG span.

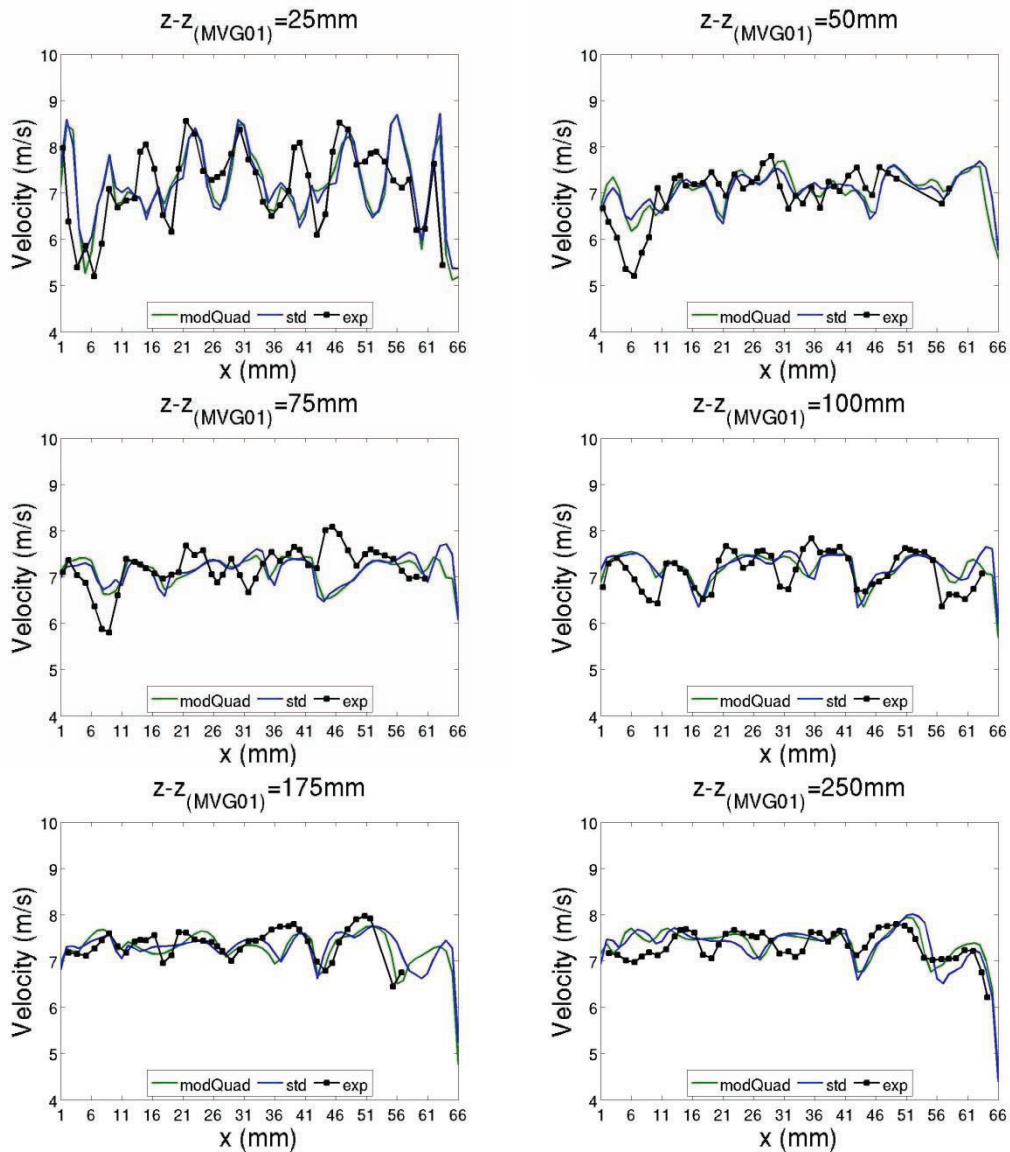


Figure 9 Mean axial velocity comparison along line 3 downstream of MVG at various elevations in spans 1a MVG and alternating SSG.

4.4.2. Mean axial velocity in the SSG span

Isotropic, anisotropic, and experimental mean axial velocities were compared along line 3 at various elevations within the core region of span 1b, as shown in Figure 10(a). Comparisons show good agreement between examined CFD calculations and experimental results in the near, intermediate, and far downstream regions. At $z - z_{(SSG)} = 235\text{mm}$, the anisotropic modified quadratic k- ϵ turbulence model exhibits better agreement than the isotropic standard k- ϵ turbulence model with respect to the measured profile. This may suggest the anisotropic turbulence model recognizes the presence of secondary flow structures [circled in Figure 11 (b)] typically found in bare-rod bundles [9]; while the isotropic turbulence model does not, as shown in Figure 11. The presence of secondary flow structures in the far wake region of the SSG (Span 1b) indicates a significant reduction in cross-flow generated by the mixing vanes (span 1a).

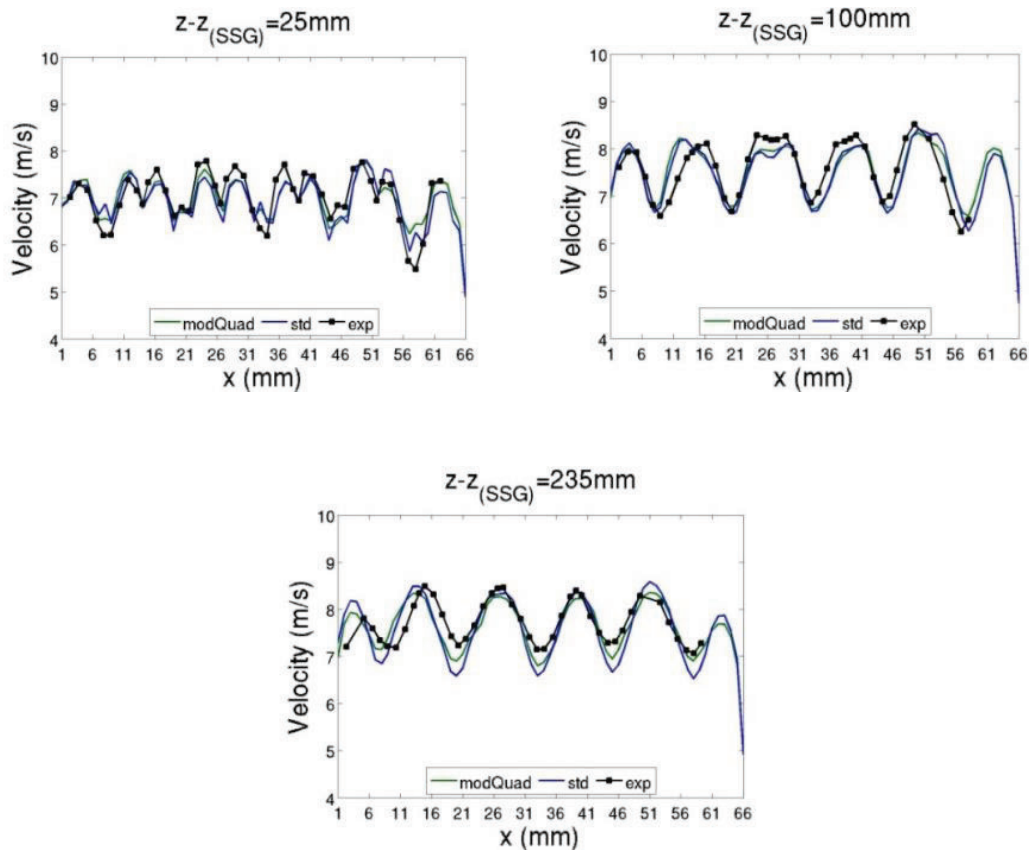


Figure 10 Mean axial velocity comparison along line 3 at various elevations in span 1b.

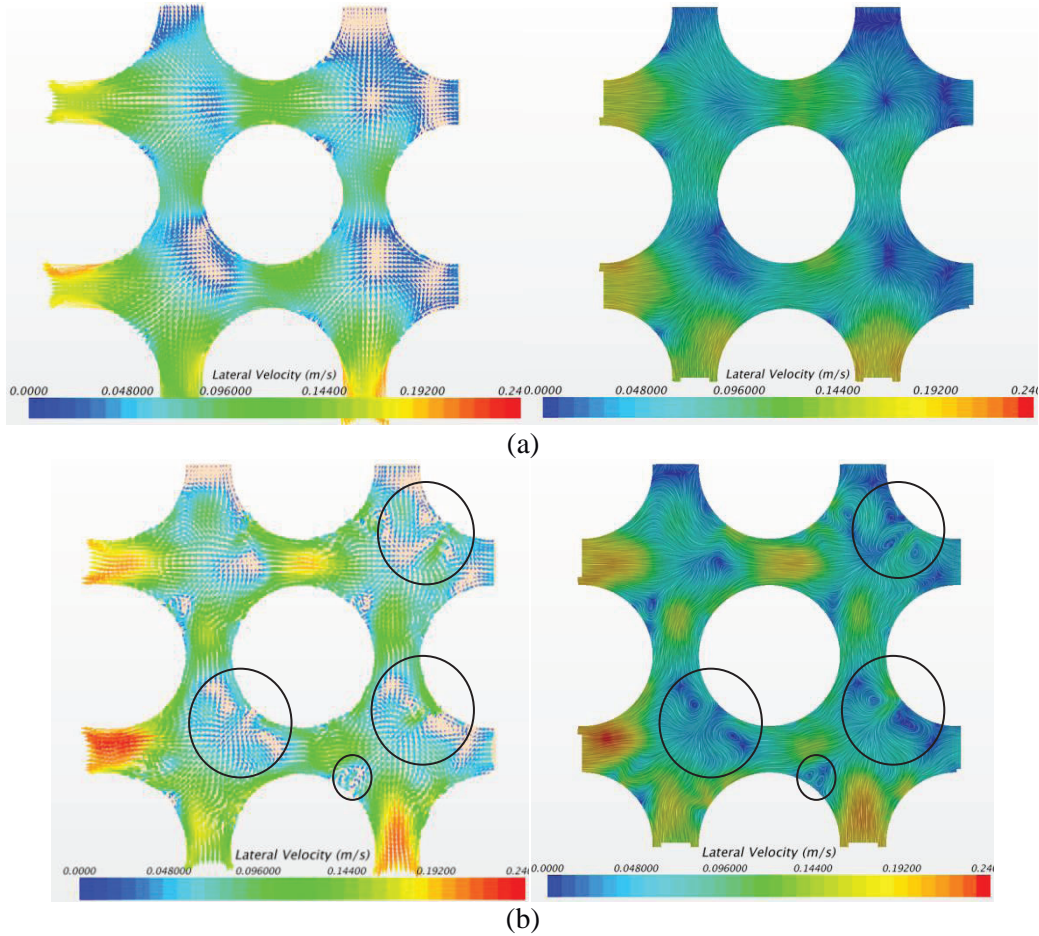


Figure 11 Mean lateral velocity field at $z - z_{(SSG)} = 235mm$ for sub-channels surrounding Rod 5 (SC15, SC16, SC21, and SC22 [Figure 4]); (a) isotropic, (b) anisotropic.

4.4.3. RMS Axial Velocity Fluctuation in the MVG span

RMS axial velocity fluctuation profiles were compared along Line 3 in the wake of the MVG span1a, as shown Figure 12. CFD-code-to-experiment comparisons show good agreement in the MVG's near wake region ($z - z_{(MVG01)} = 25mm$ and $50mm$), but CFD calculations noticeably under-predict RMS axial velocity fluctuation in the MVG's intermediate and far wake regions.

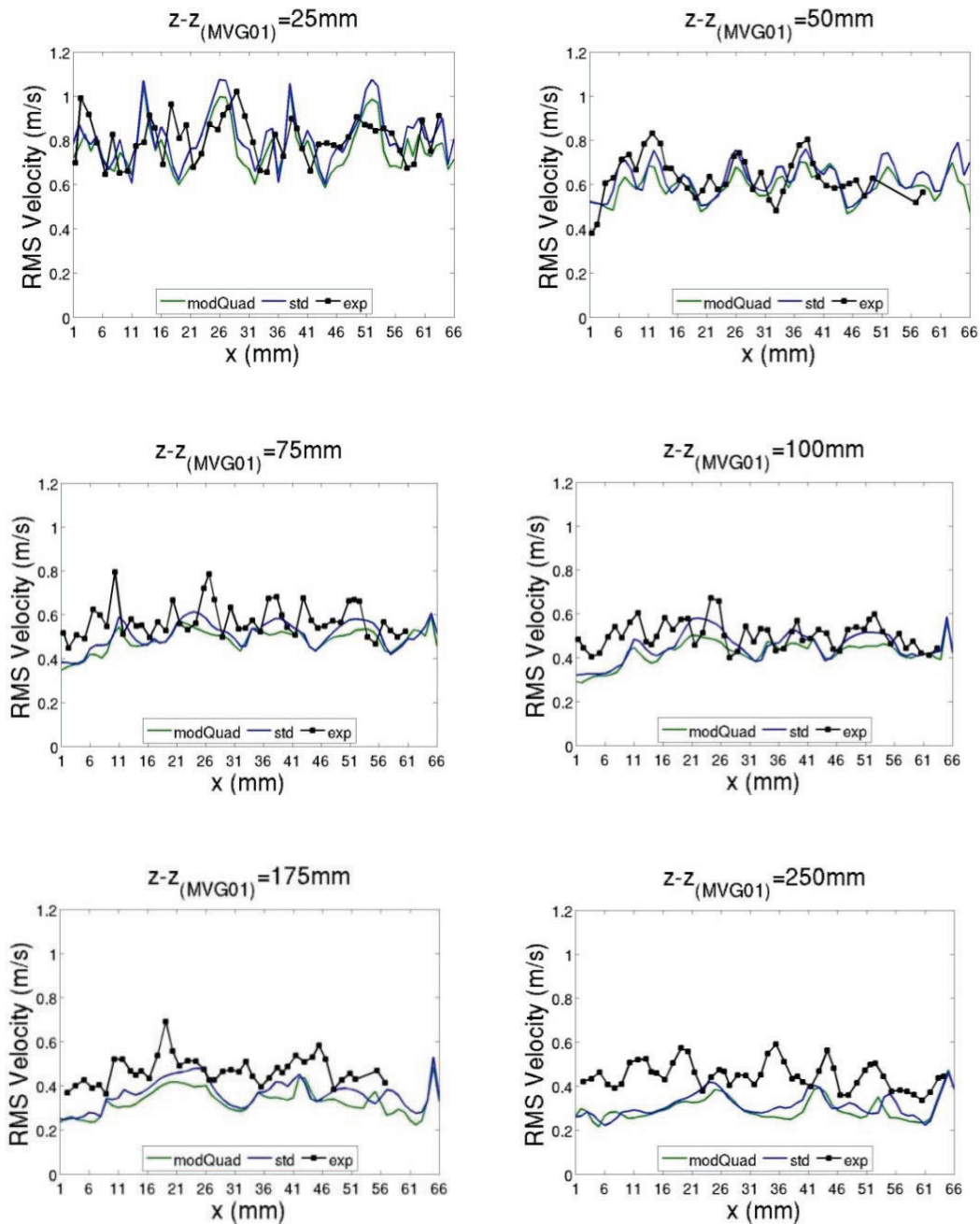


Figure 12 RMS axial velocity fluctuation comparison along line 3 at various elevations in the wake of MVG (spans 1a).

4.4.4. RMS Axial Velocity Fluctuation in the SSG span

RMS axial velocity fluctuation profiles were compared along Line 3 in the span1b wake region. All SSG wake regions under-predict RMS axial velocity fluctuation. The under-predicted trend is similar to that of the MVG span, but more pronounced within the SSG span, as shown in Figure 13.

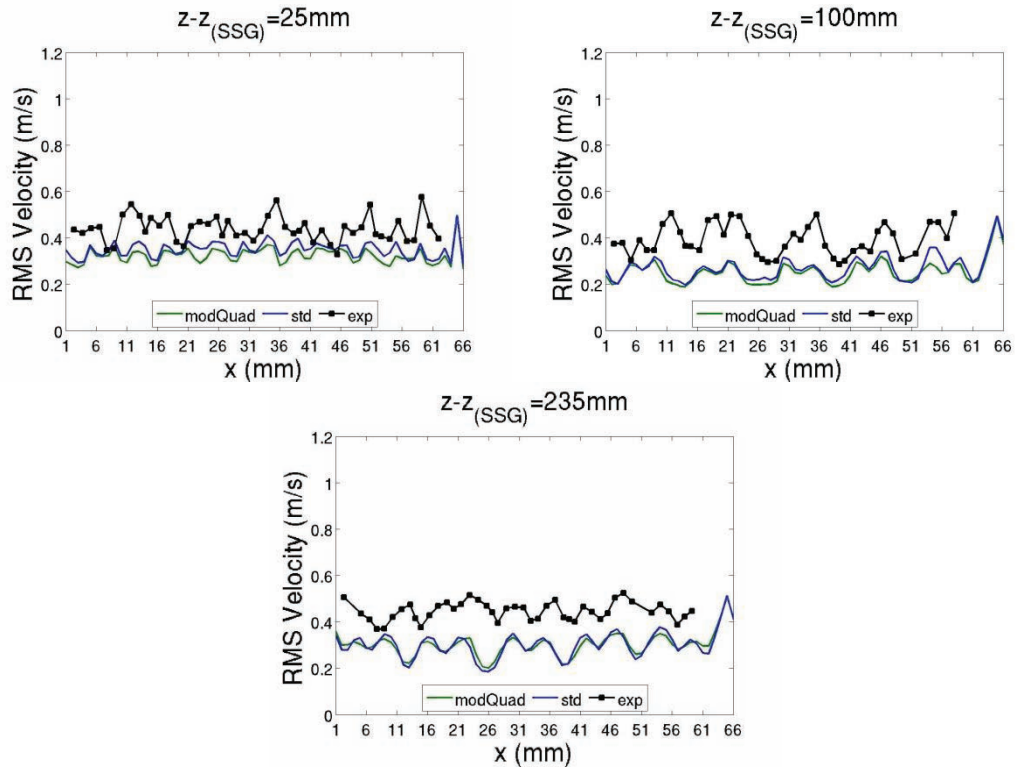


Figure 13 RMS axial velocity fluctuation comparison along line 3 at various elevations in the wake of SSG (spans 1b).

4.4.5. Axial Evolution of Secondary Flow Intensity

Secondary flow intensity exponentially decreased along the downstream MVG wake region. Upon passing the SSG (271mm to 279mm), secondary flow intensity abruptly drops (between 265mm and 285mm) by a factor of 6.53 and 4.60 for the isotropic and anisotropic turbulence models, respectively. Considering the same axial range, without the presence of the SSG, secondary flow intensity decreases by a factor of 1.08 and 1.09 for the isotropic and anisotropic turbulence models, respectively, as shown in Figure 14. Near the inlet of the downstream MVG (SSG far wake region), the secondary flow intensity is 0.014 and 0.015 for the isotropic and anisotropic turbulence models, respectively. Similarly, without the presence of the SSG, the secondary flow intensity is 0.040 and 0.033 for the isotropic and anisotropic turbulence models, respectively, as shown in Figure 14.

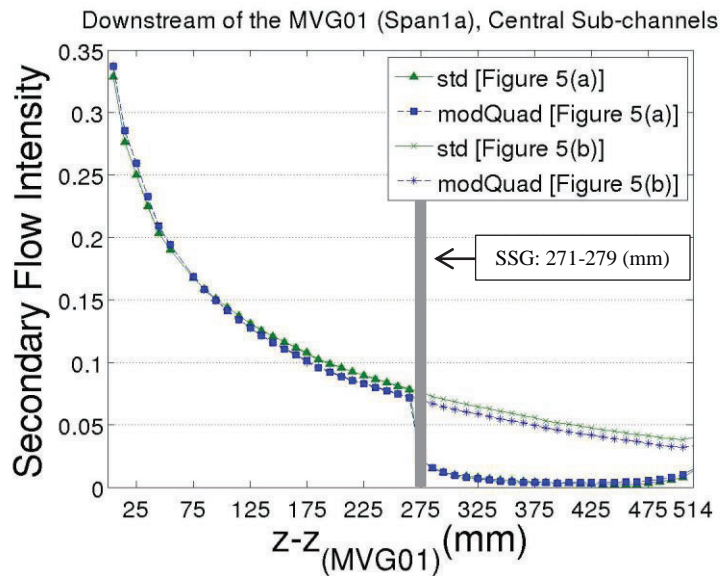


Figure 14 Central sub-channel (SC15, SC16, SC21, and SC22) average secondary flow intensity.

4.4.6. Wall Shear Stress Distribution

Comparing normalized wall shear stress distribution for Rod 5 highlights the SSG's effect on secondary flow formation in the far wake region. The examined domain considerations show similar wall shear stress distributions in the MVG wake regions, as shown in Figure 15 from 25mm to 250mm. Upon passing the SSG [Figure 15(a)], the wall shear stress distribution significantly changes from that of the upstream distribution because of the SSG, as shown in Figure 15(a). As the flow progresses along the SSG wake region, the cross-flow effect becomes smaller and the flow starts to develop fully. Thus, at the far-wake (514mm), clear differences between isotropic and anisotropic turbulence models were observed. Specifically, the isotropic turbulence model shows higher values at the rod-to-rod gap regions, while lower values are present at sub-channel center regions due to the turbulence anisotropy-driven secondary flow. On the other hand, without the SSG [Figure 15(b)], the upstream (250mm) cross-flow survived even at far-wake (514mm); thus not showing secondary flow effects, in contrast to Figure 15(a). Accordingly, the isotropic and anisotropic turbulence models show some differences in peak and valley phases but similar magnitudes of the variation.

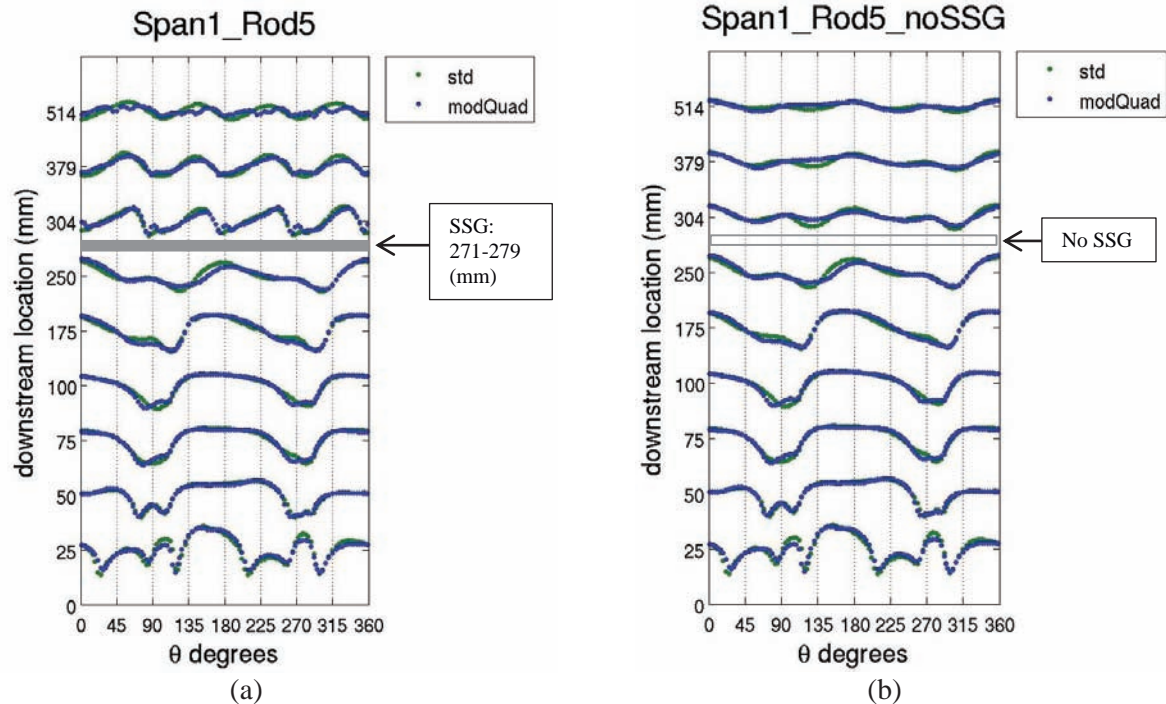


Figure 15 Normalized wall shear stresses for (a) Span 1 with MVG and SSG [Figure 5(a)], (b) Span 1 with MVG [Figure 5(b)].

5. CONCLUSIONS

Steady RANS CFD methodologies and CFD-code-to-experiment comparisons were presented for the MANIVEL-MVG bundle under isothermal conditions. Axial and global mesh size sensitivity studies identified reasonable mesh refinements for various regions of the SSG and MVG span types. CFD calculations adopted a sufficiently fine mesh and high- y^+ wall function for CFD-code-to-experiment comparisons. Examined turbulence models over predicted and slightly under predicted MVG and SSG pressure loss ratios, respectively. CFD-calculations for CFD-code-to-experiment benchmark comparisons produced comparable mean axial velocity (MVG and SSG spans) and RMS axial velocity fluctuation (MVG span) profiles.

The SSG's main purpose in the MANIVEL-MVG bundle is to stabilize the 5×5 rod array between consecutive MVGs. Differences in mean axial velocity profiles and lateral velocity vector fields between isotropic and anisotropic turbulence models indicated developing secondary flow structures in the SSG's far wake region. Further, CFD-calculations observed a sharp reduction in secondary flow intensity and abrupt re-distribution in wall shear stresses around Rod 5 upon passing the SSG. Thus, the mere inclusion of SSGs in the MANIVEL MVG bundle introduces a basic limitation for validating CFD methodologies to a general PWR MVG bundle.

Without the SSG between consecutive MVGs, secondary flow structures were not identified by the anisotropic turbulence model in the MVG's far wake region. Hence, cross-flow engendered by mixing-vanes in the actual PWR MVG bundle may be more dominant than the turbulence anisotropy-driven secondary flow, even in the MVG's far wake region. This reduces the anisotropic turbulence model's relative importance in application to the actual PWR MVG bundle.

NOMENCLATURE

A	Sub-channel area
Axial	Axial mesh length of extruded bare-rod cells
CEA	Atomic Energy and Alternative Energies Commission
CFD	Computational fluid dynamics
CHF	Critical heat flux
CILC	Crud-induced localized corrosion
CIPS	Crud-induced power shift
ρ	Density
EDF	Electricity of France
EPRI	Electric Power Research Institute
$e_a^{A\#A\#}$	Approximate relative error between two axial mesh refinements
$e_a^{B\#B\#}$	Approximate relative error between two global mesh refinements
exp	Experimental result
FI_{2nd}	Secondary flow intensity
Global	global base mesh size except for axial mesh length of extruded bare-rod cells
K	Turbulent kinetic energy
LDV	Laser-Doppler Velocimetry
ΔP_{1span}	Measured or calculated one-span pressure loss
P_{loss}	One-span pressure loss coefficient
PWR	Pressurized water reactor
MVG	Mixing vane grid (Westinghouse split-type V5H design)
modQuad	Modified quadratic k- ϵ turbulence model (anisotropic turbulence model)
RANS	Reynolds Averaged Navier-Stokes
RMS	Root mean square
SNB	Sub-cooled nucleate boiling
SSG	Simple support grid
std	Standard k- ϵ turbulence model (isotropic turbulence model)
V_0	Bulk velocity
v	Mean axial velocity
y+	Dimensionless wall distance

REFERENCES

1. *CD-adapco*, “User Guide STAR-CCM+ Version 9.04,” *STAR-CCM+ Version 9.04.009*, (2014).
2. Bergeron, A., et. al., “Design, Feasibility, and Testing of Instrumented Rod Bundles to Improve Heat Transfer Knowledge in PWR Fuel Assemblies,” *Proceeding of the 2007 International LWR Fuel Performance Meeting*, **1081**, pp. 62-68 (2007).
3. EPRI, “Computational Fluid Dynamics Benchmark of High Fidelity Rod Bundle Experiments: Industry round Robin Phase 1 – Rod Bundle with Simple Support Grids,” *Technical Report 3002000504*, Palo Alto, California, USA (2014).
4. Connor, M.E., Baglietto E., Elmahdi A.M., “CFD methodology and validation for single-phase flow in PWR fuel assemblies,” *Nuclear Engineering and Design*, **240**, pp. 2088-2095 (2010).
5. Jones, W.P., and Launder, B.E., “The Prediction of Laminarization with a Two-Equation Model of Turbulence”, *Int. J. Heat and Mass Transfer*, **15**, pp. 301-314 (1972).
6. Launder, B.E., and Sharma, B.I., “Application of the Energy Dissipation Model of Turbulence to the Calculation of Flow Near a Spinning Disc”, *Letter in Heat and Mass Transfer*, **vol. 1, no. 2**, pp 131-138 (1974).

7. Baglietto, E., Ninokata, H., Misawa T., “CFD and DNS methodologies development for fuel bundle assemblies,” *Nuclear Engineering and Design*, **236**, pp. 1503-1510 (2006).
8. SB Pope, *Turbulent Flows*, pp. 442-444, Cambridge University Press, New York, USA (2000).
9. Vonka, V., “Measurement of Secondary Flow Vortices in a Rod Bundle,” *Nuclear Engineering and Design*, **106**, pp. 191-207 (1988).